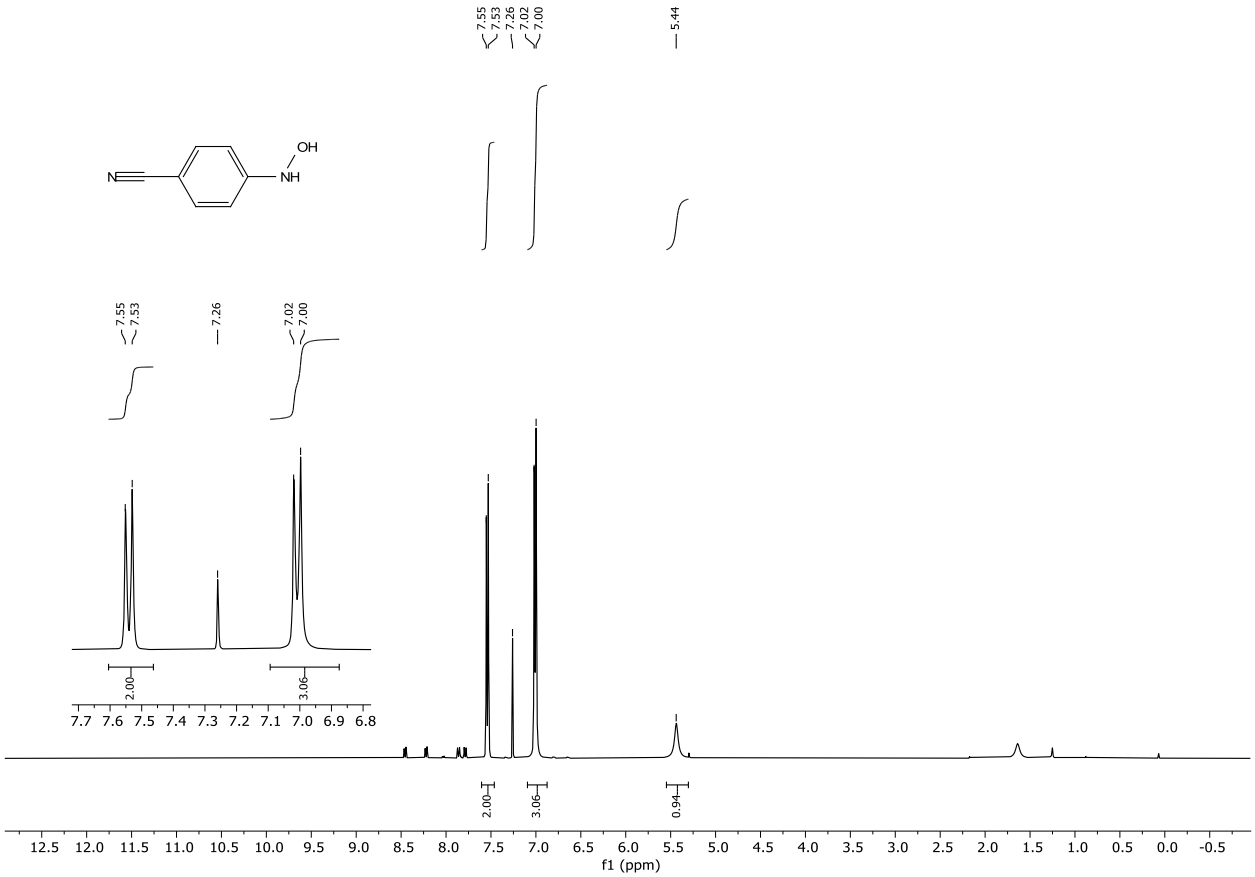

Figure S1. ^{1}H NMR of **1a** (400 MHz, $CDCl_3$).

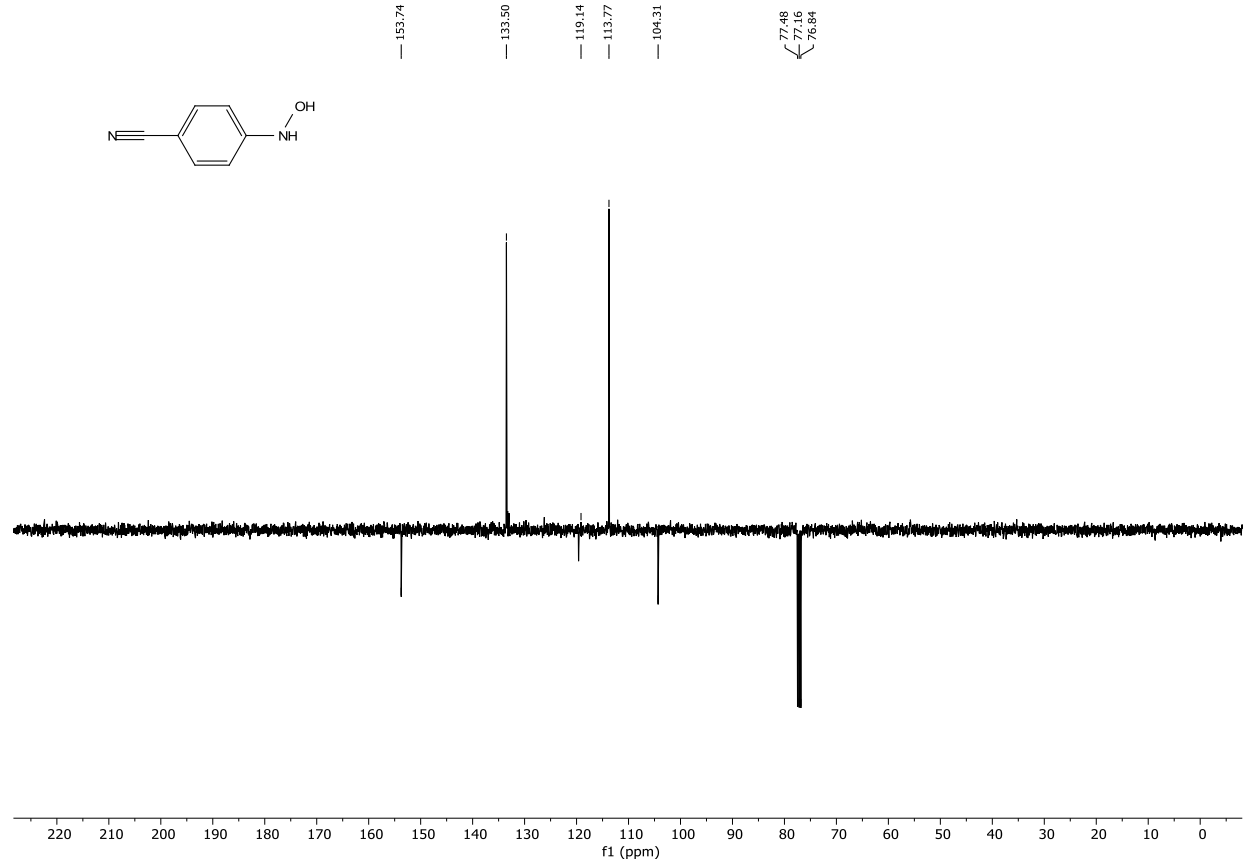

Figure S2. ^{13}C NMR of **1a** (101 MHz, $CDCl_3$).

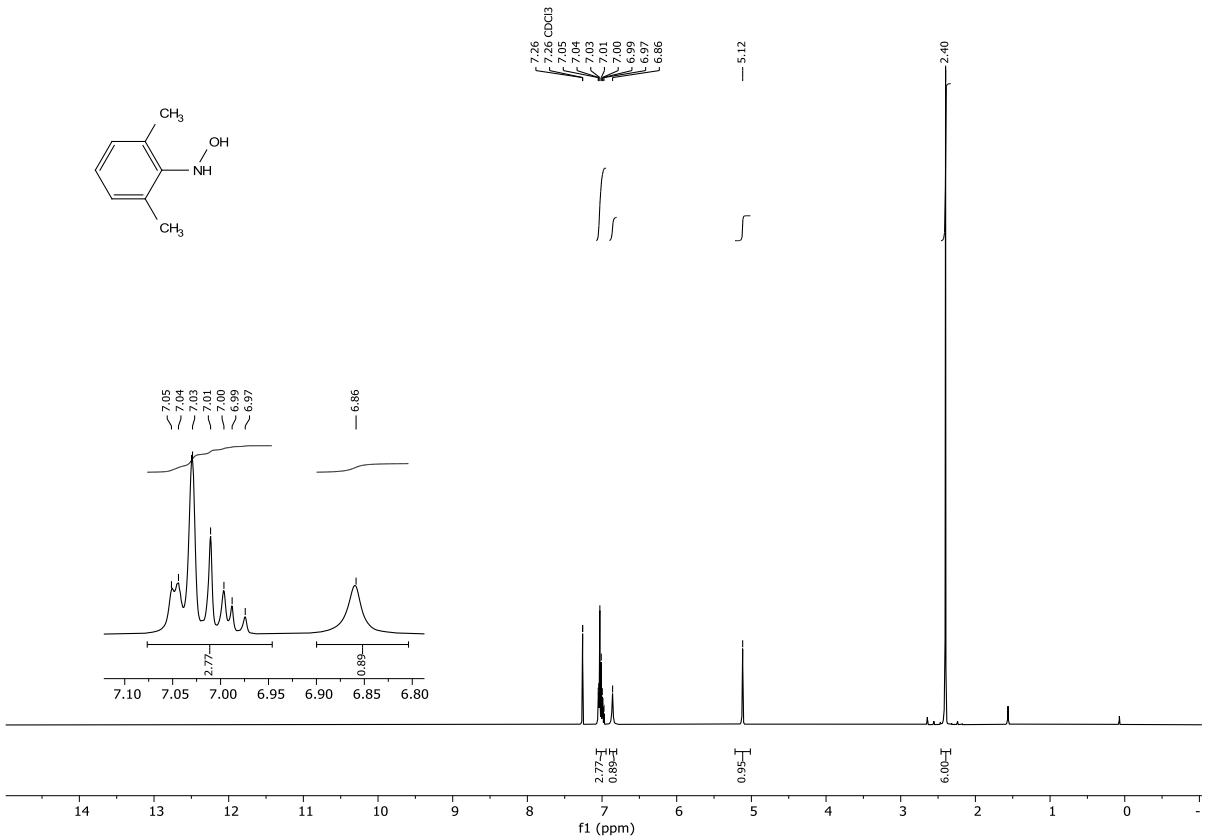

Figure S3. ^{1}H NMR of **1b**(400 MHz, $CDCl_3$).

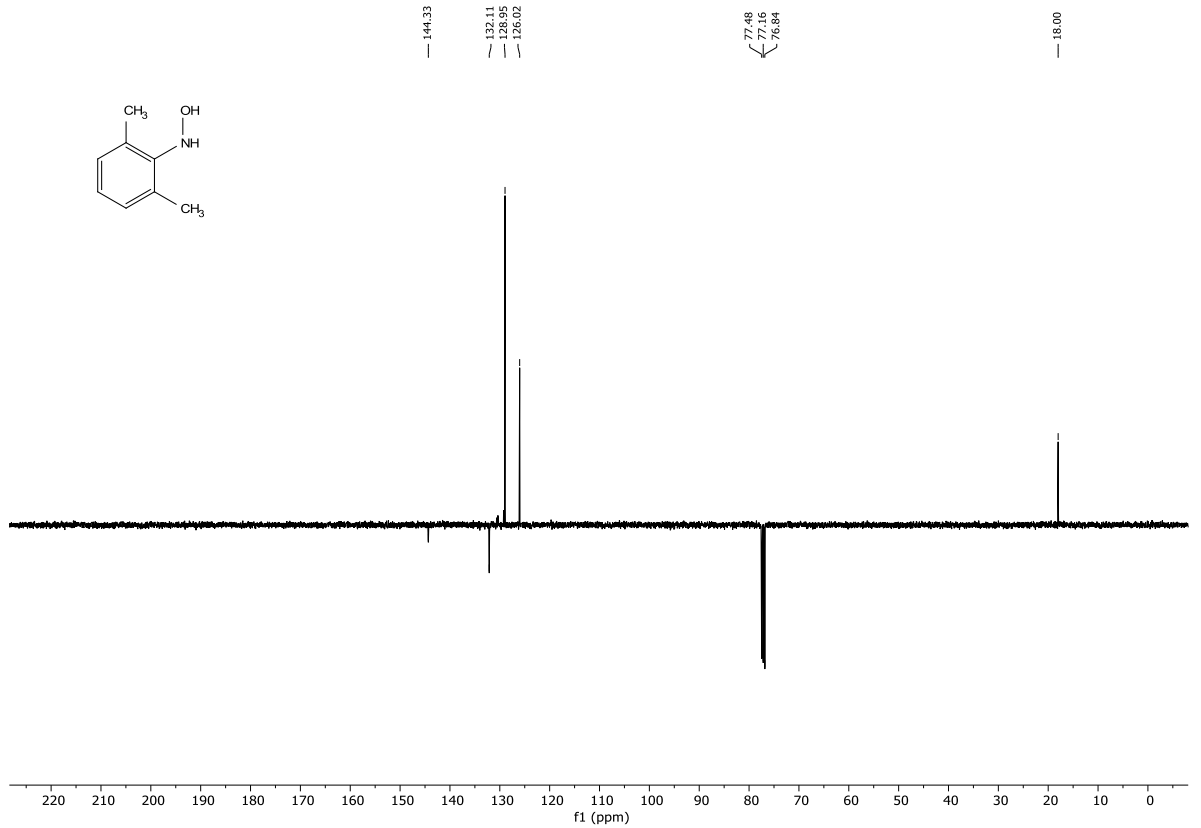

Figure S4. ^{13}C NMR of **1b** (101 MHz, $CDCl_3$).

Table S1 Crystallographic details for **2a** and results of the single crystal X-ray diffraction data collection and structural modelling.

Chemical Formula	$C_{26}H_{15}N_6OPd$
$D_{calc.}$/ g cm^{-3}	1.472
μ/mm^{-1}	6.443
Formula Weight	533.864
Colour	metallic dark green
Shape	prism
Size/mm^3	0.26×0.05×0.02
T/K	173.15
Crystal System	trigonal
Space Group	R-3
a/Å	39.7582(8)
b/Å	39.7582(8)
c/Å	7.91706(17)
α/°	90.0
β/°	90.0
γ/°	120.0
V/Å^3	10838.0(4)
Z	18
Z'	1
Wavelength/Å	1.54184
Radiation type	Cu K$_\alpha$
Θ_{min}/°	3.85
Θ_{max}/°	76.74
Measured Refl.	22785
Independent Refl.	4720
Reflections with I≥σ(I)	3890
R_{int}	0.0536
Parameters	307
Restraints	0
Largest Peak (eÅ^{-3})	0.4533
Deepest Hole (eÅ^{-3})	-0.8071
GooF	0.8174
wR_2 (all data)	0.1090
wR_2	0.1011
R_1 (all data)	0.0437
R_1	0.0343

EPR spectroscopy

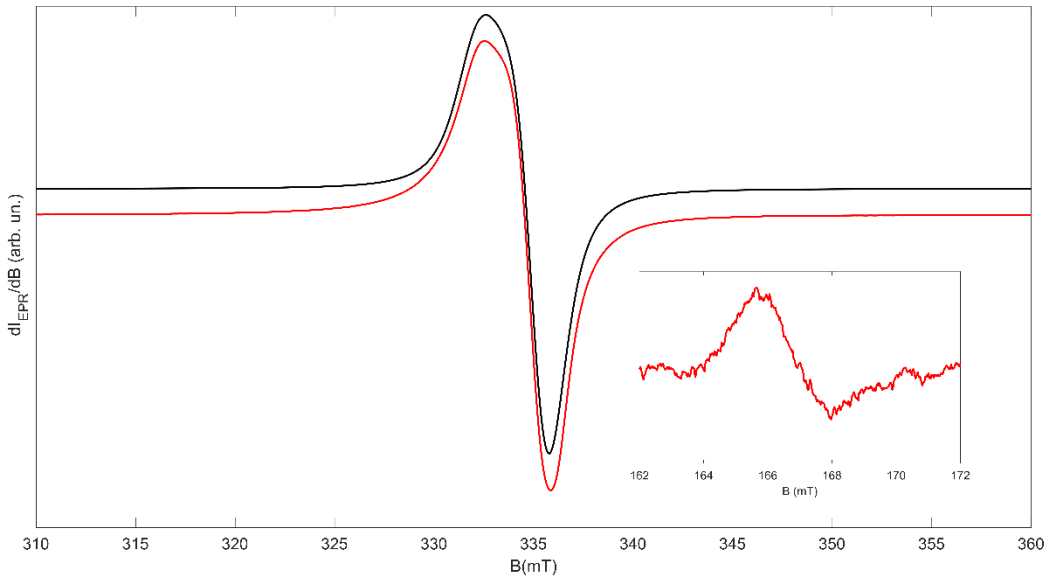

Figure S5 X-band EPR spectrum of a polycrystalline powder sample of **2a** measured at 20 K (red line) and corresponding best simulation (black line). ν= 9.3845 GHz. The inset shows the detail of the half field transition (ΔMs=±2), indicating the presence of intermolecular exchange interactions.

The parameters obtained by simulation of EPR frozen and fluid solution spectra (Table 1, main text) allowed us to decompose the hyperfine coupling tensor to the nitrogen in the traceless dipolar part and in the contact isotropic part, which are related to the spin density in s-type and p-type orbitals, respectively.[1] In this framework, the spin density on the s orbitals of the nitrogen is given by the ratio of the isotropic hyperfine coupling with the one calculated assuming the spin density residing completely in the 2s orbital of the atomic nitrogen:[2]

$$\rho_s = \frac{A_{iso}(molecule)}{A_{2s}(atom)} = \frac{26.7\ MHz}{1811\ MHz} = 0.014$$

In much the same way we can estimate the spin density residing in the Nitrogen 2p orbitals, calculating the dipolar part of the hyperfine coupling as: $^{\boldsymbol{dip}}\boldsymbol{A} = \left[A_x - \frac{T}{3}; A_y - \frac{T}{3}; A_z - \frac{T}{3}\right] = [35.4; -20.0; -15.3\ ]\ MHz$

Where *T/3*=26.8 MHz is the trace of the hyperfine tensor providing the best simulation to frozen solution spectrum of **2a**, in very good agreement with the A_{iso} value obtained by simulation of the fluid solution spectrum. By using the tabulated parameters for atomic nitrogen,[2] the spin density in the p orbital is then calculated as:

$$\rho_p = \frac{A_{iso}(molecule)}{A_{2p}(atom)} = \frac{35.4\ MHz}{111\ MHz} = 0.319$$

The analysis of the EPR spectrum then points to a spin density on the nitrogen of ca. 33.3%, in good agreement with results from calculations.

UV-VIS spectra

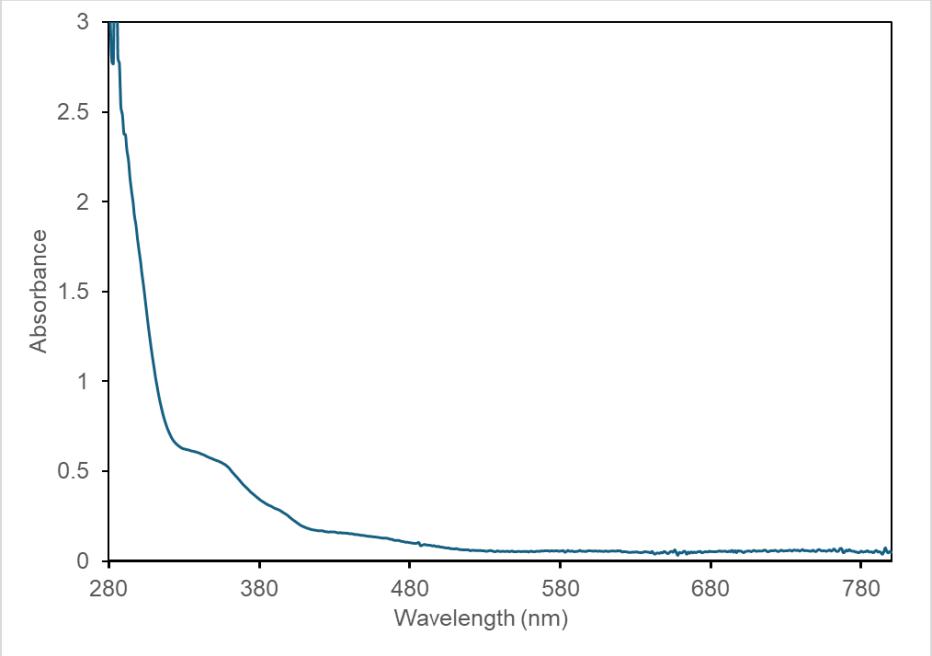

Figure S6 UV-VIS spectrum of **2a** (0.020 M) in DMF.

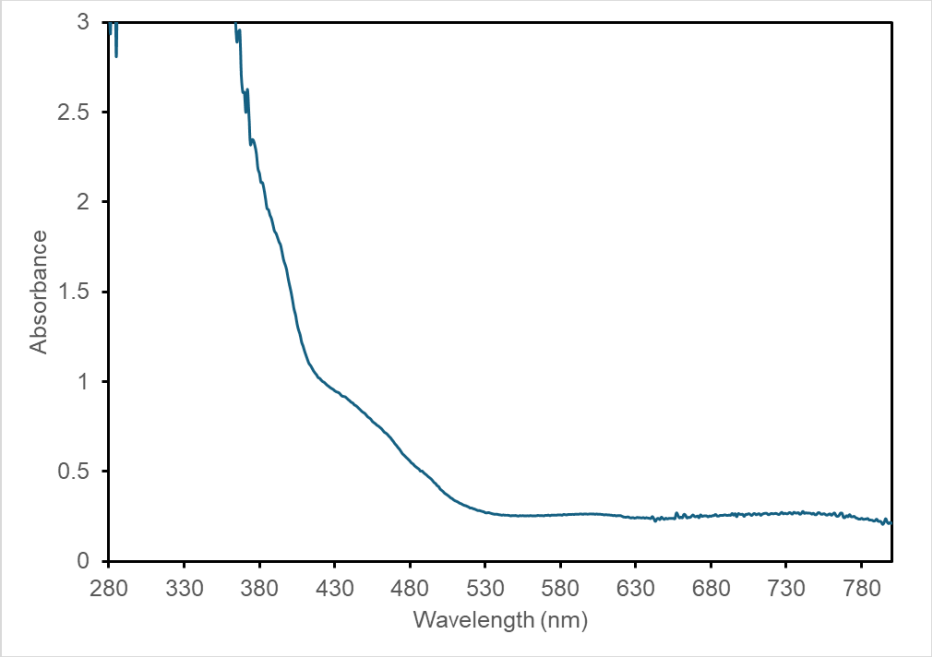

Figure S7 UV-VIS spectrum of **2a** (0.20 M) in DMF.

Computational details

Gaussian16 software[3] was used to perform geometry optimizations of the XRD species, using the uBP86 functional of Becke and Perdew[4-6] and the def2-SVP basis set,[7, 8] without dispersion. The stationary point was validated through analytical frequency calculations, which also provided zero-point energy (ZPE) and thermochemical corrections. Single-point energy refinement followed, using the uM06-D3 functional,[9, 10] with the def2-TZVPP basis set. Solvent effects of toluene were modeled using the polarization continuum model (PCM).[11]

Assignation of the metal and ligands effective oxidation states (EOS), together with the local spin analysis (LSA), was performed with the APOST-3D software using the Gaussian16 obtained wavefunctions. To evaluate the chemical bonding indicators, it is necessary to define the atom in the molecule (AIM). In this work, we used the well-established real-space Topological Fuzzy Voronoid Cells, selecting in all cases the fragments shown in Figure 4 of the main manuscript. This scheme allows a weighted partition of the space corresponding to each atom, offering results very similar to QTAIM with a reduced computational cost. All numerical integrations were performed using the default set-up defined within APOST-3D.

Computational VS XRD

To validate the DFT method the root mean square deviation (RMSD) was calculated giving RMSD= 0.261 (see **Table S2)**. An RMSD of ~0.2–0.3 Å is generally considered very small—i.e., the optimized geometry matches the experimental XRD structure extremely well, within typical experimental and computational uncertainties.

Table S2. Root mean square deviations for XRD structure and computational optimized of specie **2a**.

Atom	RMSD, Å	Atom	RMSD, Å
Pd1	0.109	C28	0.089
O2	0.227	H29	0.197
N3	0.194	C30	0.262
N4	0.052	C31	0.218
N5	0.064	H32	0.333
N6	0.156	C33	0.142
N7	0.212	C34	0.101
C8	0.042	H35	0.233
C9	0.059	C36	0.254
C10	0.117	H37	0.435
C11	0.087	C38	0.302
C12	0.065	H39	0.389
H13	0.228	C40	0.160
C14	0.159	H41	0.331
H15	0.279	C42	0.151
C16	0.114	H43	0.262
H17	0.297	C44	0.273
C18	0.059	H45	0.393
C19	0.173	C46	0.272
C20	0.120	H47	0.445
C21	0.096	C48	0.552
H22	0.133	N49	0.851
C23	0.247	All H atoms	0.306
H24	0.231	All C atoms	0.200
C25	0.062	All N atoms	0.374
H26	0.197	All O atoms	0.227
C27	0.199	All Pd atoms	0.109

Molecular orbital diagram from optimized structure.

The optimized electronic structure shows an unpaired electron in the highest energy molecular orbital (120a of Figure S8), mostly extending over the nitroso metallacycle part, albeit, with some density included in the metal center. As expected, also the three previous molecular orbitals display some kind of d-orbital composition and expand in the opposite direction to the phenanthroline (Table S3). However, as it is normal for orbitals derived from energetic DFT optimization, by means of the plot it is difficult to clearly identify which atomic orbital of the metal are contributing, at to which extent.

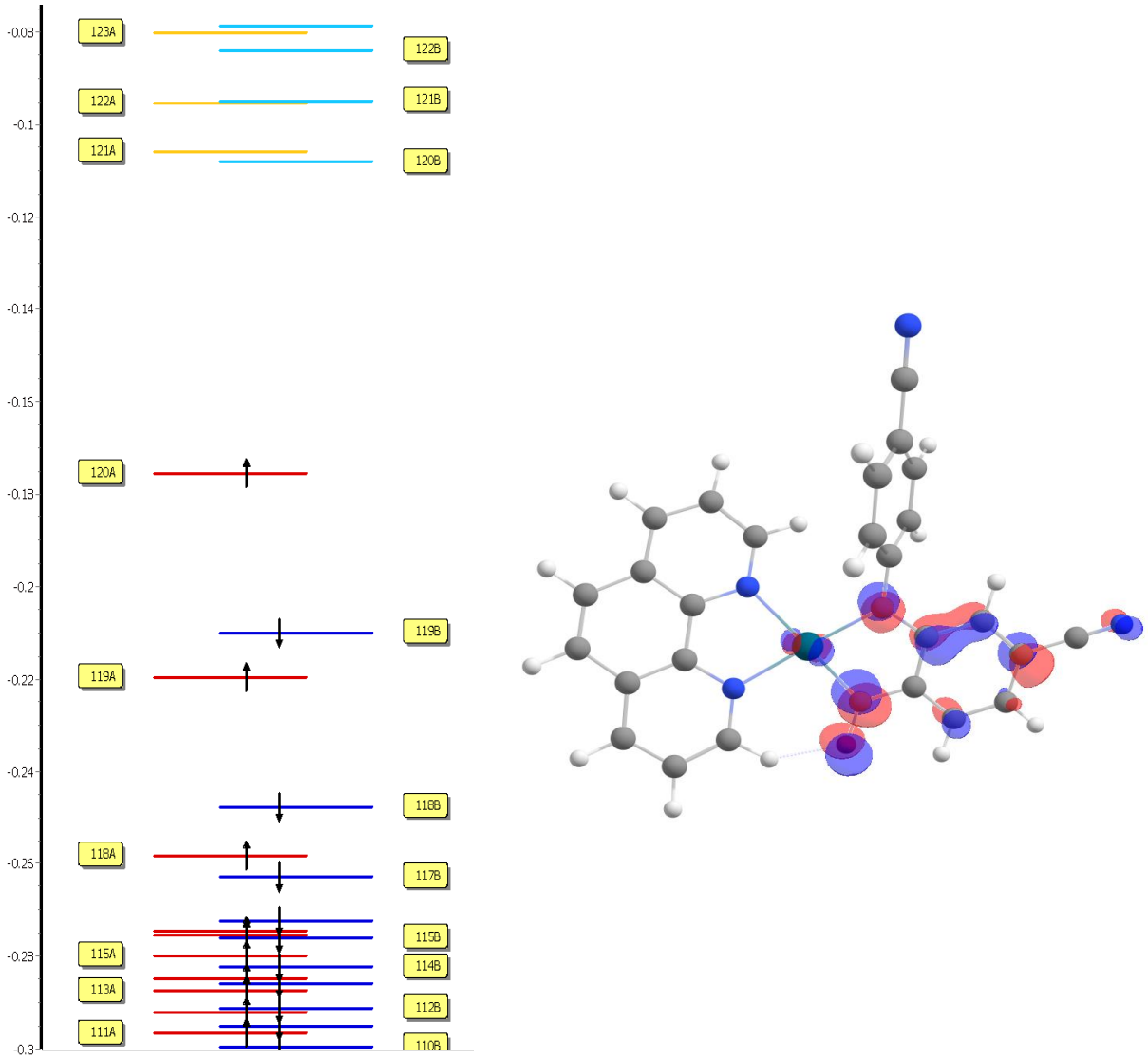

Figure S8. Orbital diagram of the optimized structure of the palladacycle and the corresponding molecular orbital of the unpaired electron (**120a**). Molecular orbitals from 120a to 116a/b are depicted in **Table S3**.

Table S3. Molecular orbitals from 120a to 116a/b of the orbital diagram reported in **Figure S9**.

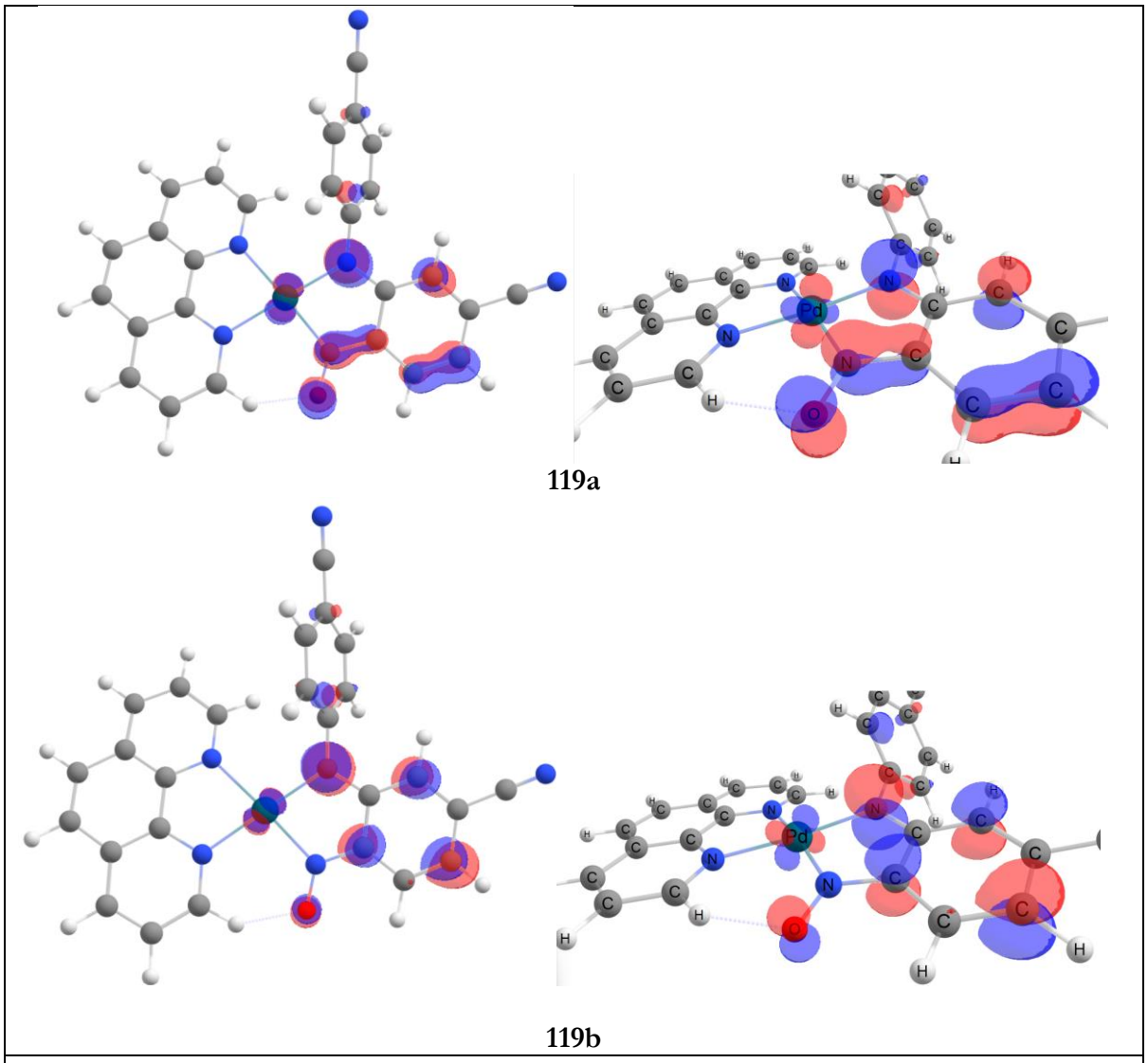

119a

119b

118a

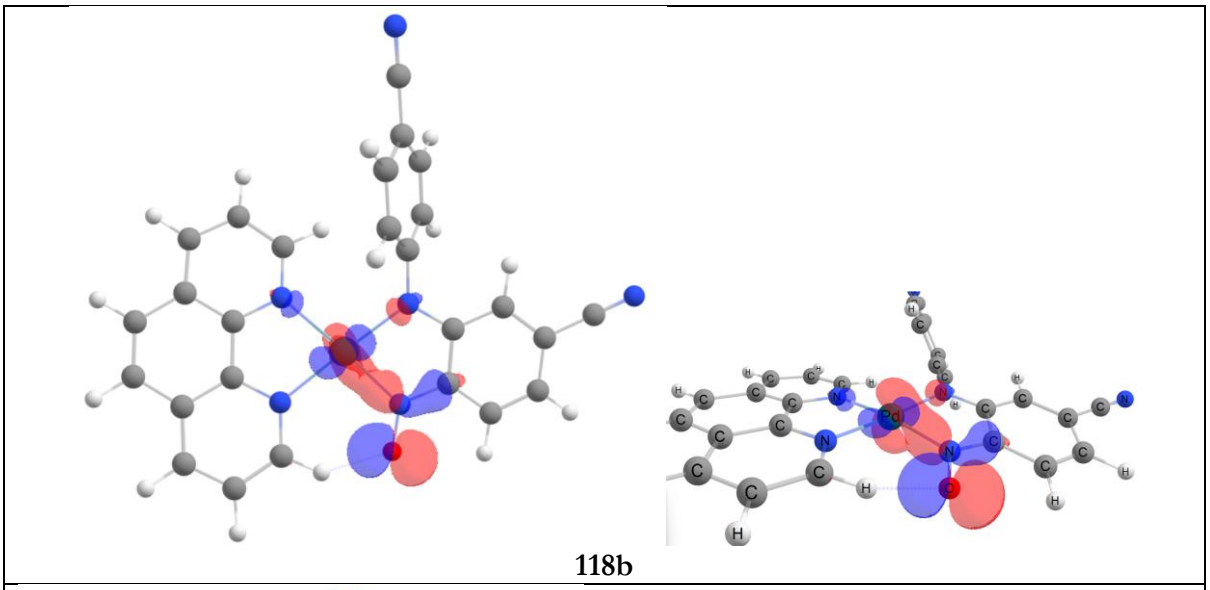

118b

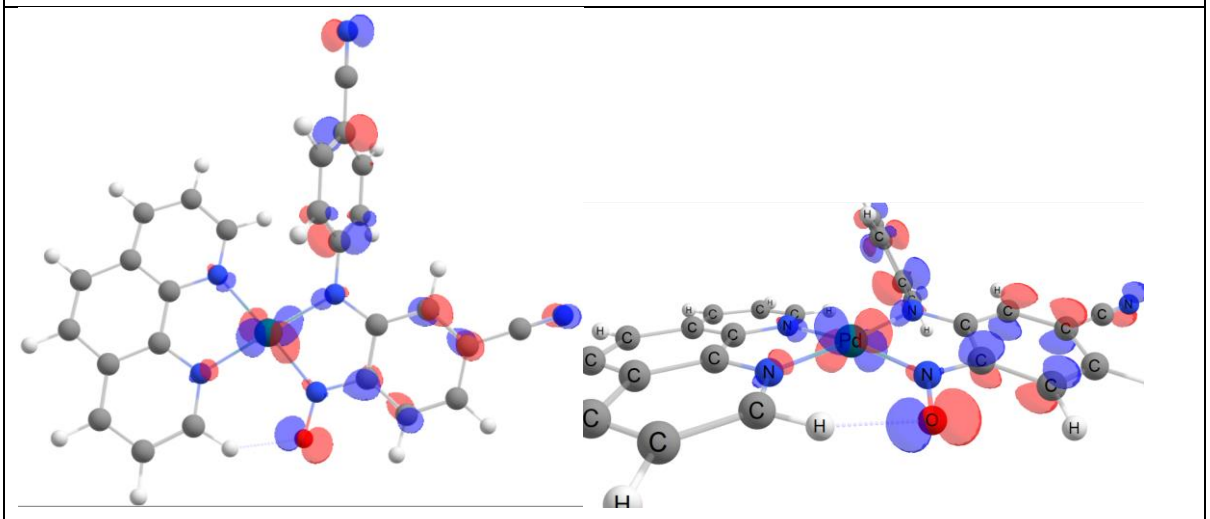

117a

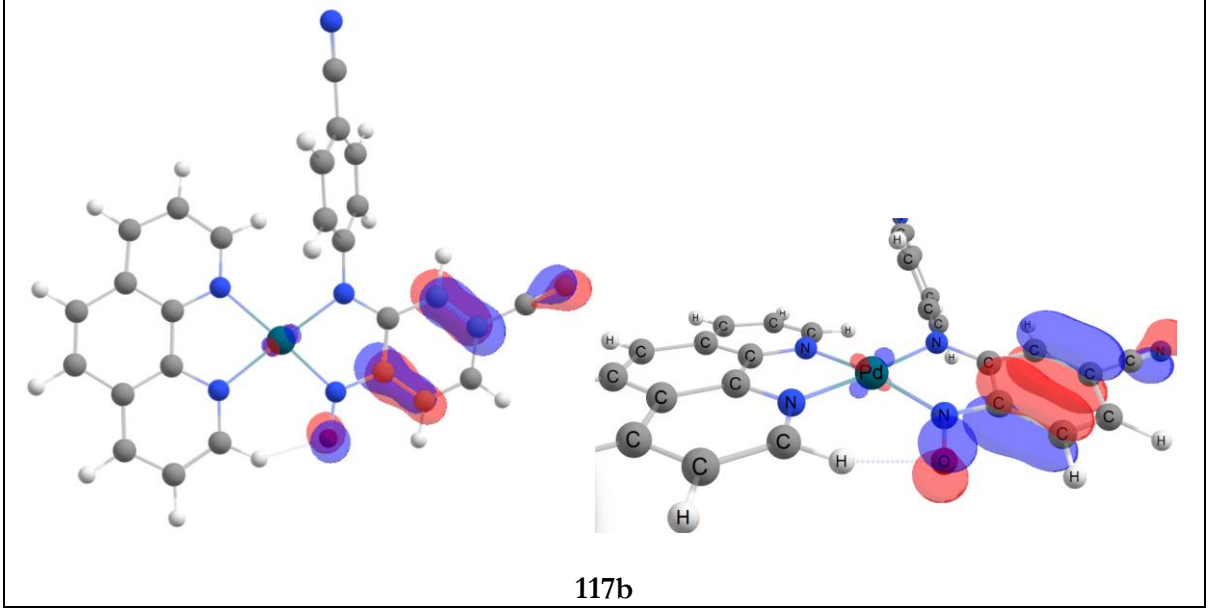

117b

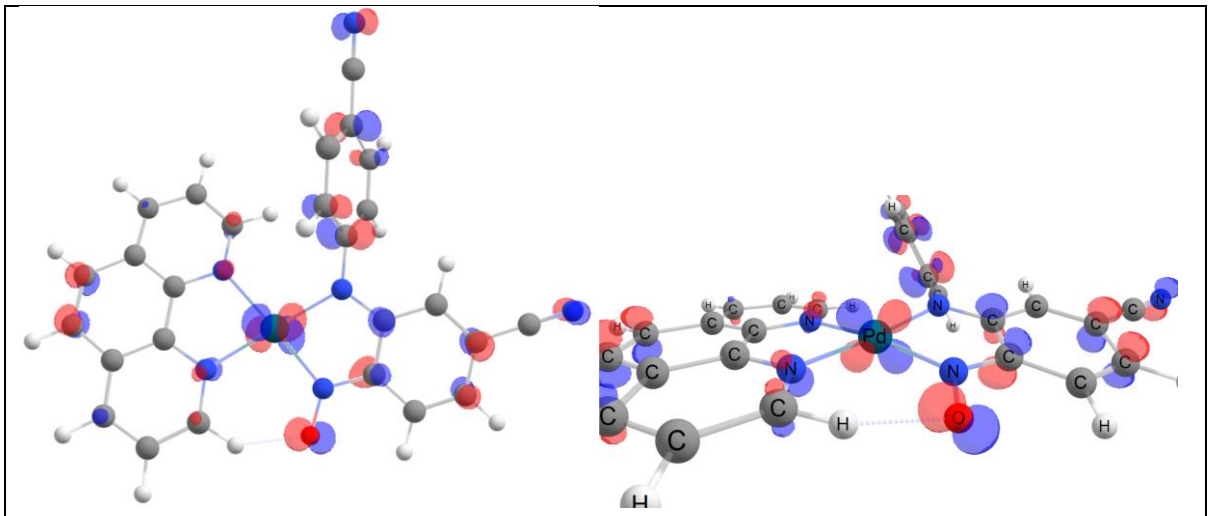

116a

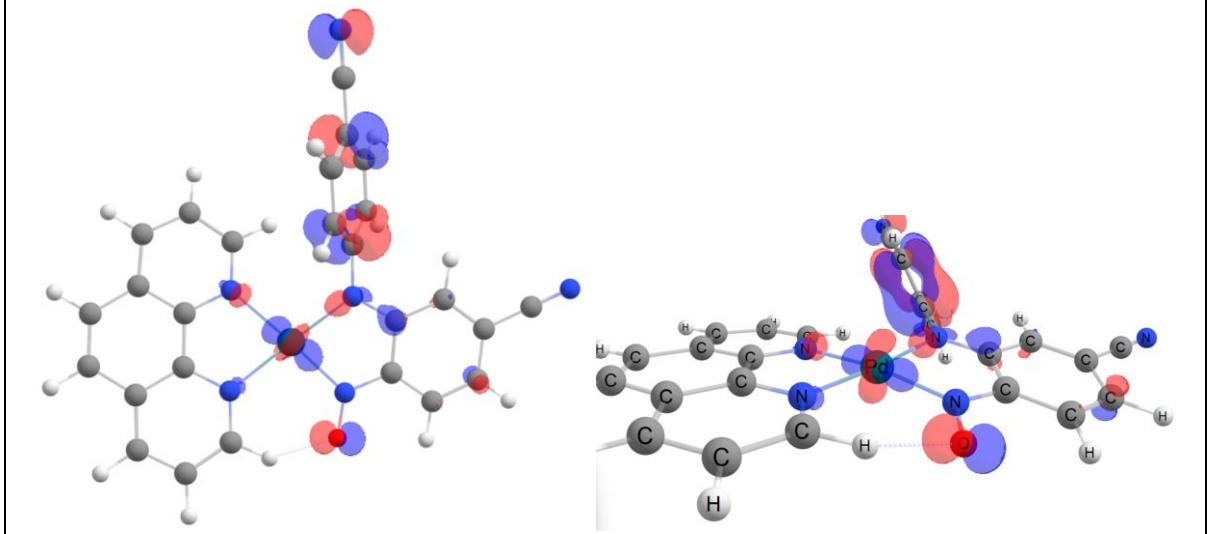

116b

Atomic Charges

Oxidation states are often written as if they were literal charges, which encourages the mistaken idea that partial atomic charges are simply their non-integer equivalents. In reality, partial charges are averaged quantities that depend strongly on the computational method and partitioning scheme, so they cannot be interpreted as "fractional oxidation states." Spin populations suffer from similar limitations: they report average spin density, and in closed-shell singlet systems they provide no meaningful guidance at all.

Having stated that, atomic charges coming from a robust real-space partition of the electronic density can provide valuable insight into bonding, reactivity, and the underlying electronic structure of a molecule. These, although they do not reflect the oxidation state of the metal center, are valuable descriptors, nevertheless.

Table S4 Atomic charges on the fragments of the metallacycle.

Fragments	3D-space (TFVC)
1	1.107
2	0.097
3	-1.208
Total	-0.004

Table S5. Atomic charges in the Topology Fuzzy Voronoi Cells (TFCV) framework on the metallacycle.

Atom	**TFVC chgs.**	**Atom**	**TFVC chgs.**
1 Pd	1.107	**26 H**	0.105
2 O	-0.647	**27 C**	0.042
3 N	-1.386	**28 C**	0.074
4 N	-1.333	**29 H**	-0.05
5 N	-1.421	**30 C**	0.15
6 N	-0.473	**31 C**	0.062
7 N	-1.235	**32 H**	-0.031
8 C	0.516	**33 C**	0.042
9 C	0.466	**34 C**	0.055
10 C	0.522	**35 H**	-0.034
11 C	0.534	**36 C**	0.096
12 C	0.084	**37 H**	-0.009
13 H	-0.06	**38 C**	0.01
14 C	0.068	**39 H**	-0.01

15	**H**	-0.023	**40**	**C**	0.073
16	**C**	0.065	**41**	**H**	-0.029
17	**H**	-0.049	**42**	**C**	0.076
18	**C**	0.132	**43**	**H**	-0.03
19	**C**	0.525	**44**	**C**	0.058
20	**C**	0.868	**45**	**H**	-0.005
21	**C**	0.056	**46**	**C**	0.058
22	**H**	-0.044	**47**	**H**	-0.011
23	**C**	0.653	**48**	**C**	0.878
24	**H**	0.001	**49**	**N**	-1.22
25	**C**	0.636			

Effective oxidation state EOS

Table S6. EFO net occupations for fragment 2, both α and β orbitals.

Net occupation for fragment 1 (α):							
0.995	0.995	0.985	0.981	0.931	0.901	0.860	0.857
0.414	0.129	0.049	0.046	0.014	0.004	0.003	0.002
0.002	0.002	0.001	0.001				
Net occupation for fragment 1 (β):							
0.995	0.995	0.985	0.981	0.931	0.904	0.868	0.857
0.387	0.128	0.049	0.046	0.029	0.004	0.003	0.002
0.002	0.002	0.001	0.001				

Table S7. EFO net occupations for fragment 2, both α and β orbitals.

Net occupation for fragment 2 (α):							
1.001	1.001	1.000	1.000	1.000	1.000	1.000	1.000
1.000	1.000	1.000	1.000	1.000	1.000	1.000	1.000
1.000	1.000	1.000	1.000	1.000	1.000	1.000	1.000
1.000	1.000	1.000	1.000	1.000	1.000	1.000	1.000
1.000	1.000	1.000	0.999	0.999	0.998	0.998	0.997
0.996	0.992	0.986	0.981	0.976	0.854	0.797	0.089
0.039	0.025	0.022	0.015	0.015	0.008	0.007	0.006
0.004	0.003	0.003	0.001				
Net occupation for fragment 2 (β):							
1.001	1.001	1.000	1.000	1.000	1.000	1.000	1.000
1.000	1.000	1.000	1.000	1.000	1.000	1.000	1.000
1.000	1.000	1.000	1.000	1.000	1.000	1.000	1.000
1.000	1.000	1.000	1.000	1.000	1.000	1.000	1.000
1.000	1.000	1.000	0.999	0.999	0.998	0.998	0.997
0.996	0.992	0.985	0.981	0.976	0.855	0.804	0.047
0.038	0.025	0.023	0.015	0.015	0.007	0.006	0.004
0.003	0.003	0.002	0.001				

Table S8. EFO net occupations for fragment 3, both α and β orbitals.

Net occupation for fragment 3 (α):							
1.001	1.000	1.000	1.000	1.000	1.000	1.000	1.000
1.000	1.000	1.000	1.000	1.000	1.000	1.000	1.000
1.000	1.000	1.000	1.000	1.000	1.000	1.000	1.000
1.000	1.000	1.000	1.000	1.000	1.000	1.000	1.000
1.000	1.000	1.000	1.000	1.000	1.000	1.000	1.000
1.000	1.000	1.000	1.000	1.000	1.000	1.000	1.000
1.000	0.999	0.999	0.998	0.997	0.997	0.996	0.994
0.993	0.992	0.990	0.987	0.975	0.959	0.921	0.827
0.641 (LO)	0.042	0.025	0.020	0.017	0.011	0.011	0.005
0.004	0.003	0.001	0.001				
Net occupation for fragment 3 (β):							
1.001	1.000	1.000	1.000	1.000	1.000	1.000	1.000
1.000	1.000	1.000	1.000	1.000	1.000	1.000	1.000
1.000	1.000	1.000	1.000	1.000	1.000	1.000	1.000
1.000	1.000	1.000	1.000	1.000	1.000	1.000	1.000
1.000	1.000	1.000	1.000	1.000	1.000	1.000	1.000
1.000	1.000	1.000	1.000	1.000	1.000	1.000	1.000
1.000	0.999	0.999	0.998	0.997	0.997	0.996	0.994
0.993	0.990	0.989	0.976	0.973	0.955	0.825	0.604 (LO)
0.051	0.041	0.022	0.017	0.011	0.011	0.005	0.004
0.003	0.001	0.001					

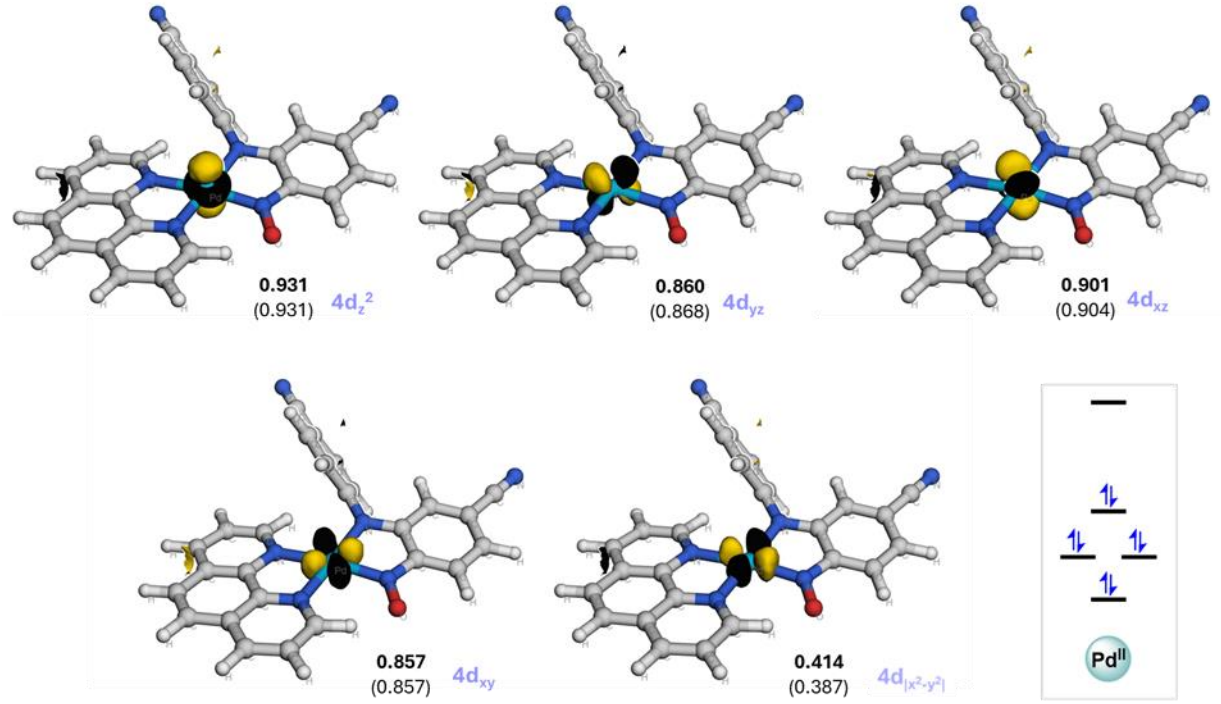

Figure S9. EFO valence d orbitals of the metal center. Orbital occupation of α (**bold**) and β (in parenthesis) electrons is reported.

Local Spin Analysis (LSA)

Table S9. Effective number of unpaired electrons, and its percentage.

Fragment	no. eff. unpaired elec.	Percent. (%)
1	0.043	4.05%
2	0.048	4.52%
3	0.971	91.43%
Total	1.062	100%

Table S10. Major percentages of the effectively unpaired electron on the original system and on the cyanide-free analog.

		para-CN	%	para-H	%
N	**6**	0.312	**29.4%**	0.314	**29.7%**
O	**2**	0.296	**27.9%**	0.274	**25.9%**
C	**18**	0.075	**7.0%**	0.071	**6.8%**
C	**14**	0.073	**6.9%**	0.071	**6.7%**
C	**8**	0.057	**5.3%**	0.056	**5.3%**
Pd	**1**	0.043	**4.1%**	0.044	**4.2%**
...		...	**…**	**...**	**...**
Sum Pop		1.062	**100%**	1.058	**100%**

Table S11. Decomposition of $< S^2 >$ over the three fragments and final total value.

Fragments/Fragments	1	2	3
1	0.032	-0.001	-0.009
2	-0.001	0.035	0.000
3	-0.009	0.000	0.733
Total:			0.781

Computational EPR Simulation

The simulation of the EPR spectra was ran with ORCA, maintaining the same model as for the single-point calculation. However, to properly account for the property calculations, relativistic effects were accounted by replacing all the basis-sets for ZORA-def2-TZVP, and the effective-core potential of

the metal centre by the SARC-ZORA-TZVP to also account for all electrons. These changes follow ORCA's EPR recommendations that, specifically for EPR hyperfine, geometry/energy basis sets are often not satisfactory, especially for heavier atoms, because core-region flexibility matters. Below the input used is copied, followed by the main EPR related output values (SARC-ZORA-TZVP for the metal centre, and ZORA-def2-TZVP for the other atoms):

```
! UKS M06 EPR-III D4 ZORA DEFGRID3 TightSCF
! CPCM(toluene)
%pal
  nprocs 1
end
%maxcore 5000
%basis
  NewGTO P  "ZORA-def2-TZVP" end
  NewGTO C  "ZORA-def2-TZVP" end
  NewGTO H  "ZORA-def2-TZVP" end
  NewGTO N  "ZORA-def2-TZVP" end
  NewGTO O  "ZORA-def2-TZVP" end
  NewGTO Pd "SARC-ZORA-TZVP" end
end

%scf MaxIter 500
      LShift 0.5
      end

%output
      Print[P_Basis] 2
      Print[P_MOs] 1
end

%plots
dim1 120
dim2 120
dim3 120
Format Gaussian_Cube
SpinDens ("epr_pd1_sd.cube");
ElDens ("epr_pd1_ed.cube");
end

* xyz 0 2
Pd     -0.509042965    -0.798910138    -0.038224334
O      -0.162051497    -3.700331674     0.020311569
N      -1.580961043     1.003008691    -0.374034207
N       1.440369898    -0.162739176     0.008468186
N      -2.466087331    -1.468221873     0.146249367
N       0.418666019    -2.582543517    -0.003520753
N       7.180042864    -1.946996613    -0.134263035
C       2.351522298    -1.185085496    -0.071964564
C       1.844751203     1.174691148     0.142368895
C       1.801758446    -2.515123456    -0.097931263
C      -3.412993809    -0.470822679     0.067994629
```

```
C       3.765466196    -1.063707158    -0.059289729
H       4.236737606    -0.074368550     0.013108371
C       2.627665339    -3.667384595    -0.170665123
H       2.144875566    -4.653874161    -0.195195998
C       1.442006776     1.920546064     1.281648966
H       0.848287238     1.411581016     2.056288908
C       4.582438222    -2.214252016    -0.130489694
C      -2.944732265     0.843190843    -0.232120668
C       6.009426535    -2.064919181    -0.130942987
C       2.619632291     1.828721429    -0.853304040
H       2.924150683     1.267479198    -1.749815788
C      -1.128400225     2.209961098    -0.765859711
H      -0.043138203     2.303199393    -0.912882206
C      -2.865988018    -2.724806359     0.407254828
H      -2.047259954    -3.470334477     0.431436299
C      -3.874916726     1.916590972    -0.402638192
C       4.009464513    -3.522579427    -0.198489371
H       4.667643528    -4.401116400    -0.259355519
C       2.558495406     3.915152316     0.420236371
C       2.974139031     3.175614870    -0.717165186
H       3.566695130     3.673298522    -1.499775384
C      -4.808366422    -0.724278683     0.246809455
C       1.788824343     3.267282049     1.421105634
H       1.473609786     3.831844576     2.311627017
C      -4.222326850    -3.052579689     0.610147914
H      -4.489417800    -4.098092547     0.823295493
C      -1.977559785     3.314839542    -0.975209735
H      -1.535506495     4.272065293    -1.287742691
C      -5.724225610     0.381443898     0.112917005
H      -6.799544737     0.191402213     0.257239484
C      -5.277358670     1.645146825    -0.204109052
H      -5.991874625     2.475481614    -0.319210129
C      -3.356021417     3.181866020    -0.774557745
H      -4.036378494     4.036227499    -0.915508100
C      -5.201690218    -2.056703778     0.531515493
H      -6.267007900    -2.293875459     0.679559136
C       2.902428512     5.302557228     0.552373628
N       3.173667106     6.441696930     0.657806633
*

%eprnmr
      gtensor true printlevel 3
      ori CenterOfElCharge
      Nuclei = all N {aiso, adip}
      Nuclei = all O {aiso, adip}
      Nuclei = all Pd {aiso, adip}
      Nuceli = all H {aiso, adip}

end
```

The computed g-tensor exhibits only moderate anisotropy, with principal values g_x=1.9880, g_y=1.9963, and g_z=2.0148(g_"iso" =1.9997), remaining close to the free-electron value. This indicates limited spin–orbit coupling and, with agreement with the other analysis tools used, it argues against a predominantly metal-centered unpaired electron (i.e. Pd(I)). In the same line, calculated hyperfine coupling constants reveal that the largest interactions are associated with the nitroso part of the ligand. In particular, the oxygen nucleus displays a highly anisotropic tensor with one large principal component (A_x=-137.4 MHz) and significantly smaller perpendicular components, characteristic of substantial spin density localized in a directional p-type orbital. The nitrogen atom also exhibits a pronounced hyperfine interaction (A_x=63.2 MHz). In contrast, the palladium centre displays relatively small hyperfine values (of the order of 5–11 MHz), indicating only limited spin delocalization onto the metal.

Further analysis involved spin population analysis, which confirms the ligand-centered nature of the unpaired electron. The spin density is predominantly localized on the nitroso fragment, with significant contributions on both the oxygen (≈0.31) and the coordinated nitrogen atom (≈0.30), largely residing in p-type orbitals. In particular, the dominant contribution arises from p_z orbitals on both atoms, indicating that the unpaired electron occupies a π* orbital delocalized over the N–O unit. In contrast, the palladium centre carries only a negligible spin population (≈0.02), arising mainly from minor spin polarization effects rather than true spin localization.

Together with the near-isotropic g-values close to the free-electron value, these results unequivocally support a description of the complex as a Pd(II) center bound to a non-innocent nitroso ligand bearing the majority of the unpaired spin density.

Table S12. Euler rotation of hyperfine tensor to g-tensor.

	Ax	Ay	Az
N3	-4.19	-4.53	-3.87
N4	1.26	-2.22	-1.77
N5	-1.13	-1.04	-1.47
N6	**63.17**	**9.37**	**7.33**
N7	8.96	1.05	0.53
N49	0.00	0.09	0.02
O2	**-137.42**	**8.25**	**21.07**
Pd1	**-5.79**	**5.90**	**11.03**
H13	-1.40	-0.10	1.86
H15	**-16.62**	**-15.60**	**-9.49**
H17	-1.13	0.90	-0.57
H22	-0.59	-0.50	1.32
H24	-1.84	-0.65	-1.34
H26	**-4.41**	**-4.89**	**7.63**
H29	4.85	4.36	9.72
H32	-0.19	-0.09	0.50
H35	-0.22	0.42	-0.20
H37	-0.66	-0.60	1.04
H39	-0.22	0.41	-0.13
H41	-0.10	0.37	-0.05
H43	-0.16	0.22	-0.08
H45	-1.35	-0.37	-1.85
H47	-1.24	-1.61	-0.13

Cartesian coordinates of complex 2a DFT optimized structure

49

Pd	-0.50904	-0.79891	-0.03822
O	-0.16205	-3.70033	0.02031
N	-1.58096	1.00301	-0.37403
N	1.44037	-0.16274	0.00847
N	-2.46609	-1.46822	0.14625
N	0.41867	-2.58254	-0.00352
N	7.18004	-1.94700	-0.13426
C	2.35152	-1.18509	-0.07196
C	1.84475	1.17469	0.14237
C	1.80176	-2.51512	-0.09793
C	-3.41299	-0.47082	0.06799
C	3.76547	-1.06371	-0.05929
H	4.23674	-0.07437	0.01311
C	2.62767	-3.66738	-0.17067
H	2.14488	-4.65387	-0.19520
C	1.44201	1.92055	1.28165
H	0.84829	1.41158	2.05629
C	4.58244	-2.21425	-0.13049
C	-2.94473	0.84319	-0.23212
C	6.00943	-2.06492	-0.13094
C	2.61963	1.82872	-0.85330
H	2.92415	1.26748	-1.74982
C	-1.12840	2.20996	-0.76586
H	-0.04314	2.30320	-0.91288
C	-2.86599	-2.72481	0.40725
H	-2.04726	-3.47033	0.43144
C	-3.87492	1.91659	-0.40264
C	4.00946	-3.52258	-0.19849
H	4.66764	-4.40112	-0.25936
C	2.55850	3.91515	0.42024
C	2.97414	3.17561	-0.71717
H	3.56670	3.67330	-1.49978
C	-4.80837	-0.72428	0.24681
C	1.78882	3.26728	1.42111
H	1.47361	3.83184	2.31163
C	-4.22233	-3.05258	0.61015
H	-4.48942	-4.09809	0.82330
C	-1.97756	3.31484	-0.97521
H	-1.53551	4.27207	-1.28774
C	-5.72423	0.38144	0.11292
H	-6.79954	0.19140	0.25724
C	-5.27736	1.64515	-0.20411
H	-5.99187	2.47548	-0.31921
C	-3.35602	3.18187	-0.77456
H	-4.03638	4.03623	-0.91551
C	-5.20169	-2.05670	0.53152
H	-6.26701	-2.29388	0.67956
C	2.90243	5.30256	0.55237
N	3.17367	6.44170	0.65781

References

1. J. A. Weil, J. R. Bolton, Electron Paramagnetic Resonance: Elementary Theory and Practical Applications. John Wiley & Sons, Inc., Hoboken, New Jersey 2007
2. J. R. Morton and K. F. Preston, *J. Magn. Reson. (1969)*, 1978, **30**, 577–582.
3. M. J. Frisch, G. W. Trucks, H. B. Schlegel, G. E. Scuseria, M. A. Robb, J. R. Cheeseman, G. Scalmani, V. Barone, G. A. Petersson, H. Nakatsuji, X. Li, M. Caricato, A. V. Marenich, J. Bloino, B. G. Janesko, R. Gomperts, B. Mennucci, H. P. Hratchian, J. V. Ortiz, A. F. Izmaylov, J. L. Sonnenberg, Williams, F. Ding, F. Lipparini, F. Egidi, J. Goings, B. Peng, A. Petrone, T. Henderson, D. Ranasinghe, V. G. Zakrzewski, J. Gao, N. Rega, G. Zheng, W. Liang, M. Hada, M. Ehara, K. Toyota, R. Fukuda, J. Hasegawa, M. Ishida, T. Nakajima, Y. Honda, O. Kitao, H. Nakai, T. Vreven, K. Throssell, J. A. Montgomery Jr., J. E. Peralta, F. Ogliaro, M. J. Bearpark, J. J. Heyd, E. N. Brothers, K. N. Kudin, V. N. Staroverov, T. A. Keith, R. Kobayashi, J. Normand, K. Raghavachari, A. P. Rendell, J. C. Burant, S. S. Iyengar, J. Tomasi, M. Cossi, J. M. Millam, M. Klene, C. Adamo, R. Cammi, J. W. Ochterski, R. L. Martin, K. Morokuma, O. Farkas, J. B. Foresman and D. J. Fox, *Gaussian 16 Rev. C.01*, Wallingford, CT, 2016.
4. A. D. Becke, *Physical Review A*, 1988, **38**, 3098–3100.
5. J. P. Perdew, *Phys. Rev. B*, 1986, **33**, 8822–8824.
6. J. P. Perdew, *Phys. Rev. B*, 1986, **34**, 7406–7406.
7. F. Weigend and R. Ahlrichs, *Phys. Chem. Chem. Phys.*, 2005, **7**, 3297–3305.
8. F. Weigend, *Phys. Chem. Chem. Phys.*, 2006, **8**, 1057–1065.
9. Y. Zhao and D. G. Truhlar, *Theor. Chem. Acc.*, 2008, **120**, 215–241.
10. S. Grimme, J. Antony, S. Ehrlich and H. Krieg, *J. Chem. Phys.*, 2010, **132**.
11. G. Scalmani and M. J. Frisch, *J. Chem. Phys.*, 2010, **132**.